LANGMUIR

pubs.acs.org/Langmuir Article

Tunable Spontaneous Droplet Motion in Flexible Channels

Haiyi Zhong, Zhongzheng Wang,* Si Suo, Leila Mamizadeh Janghour, Behnam Akhavan, and Yixiang Gan*

Cite This: *Langmuir* 2025, 41, 7355−7363 Read Online

ACCESS | Metrics & More | Article Recommendations

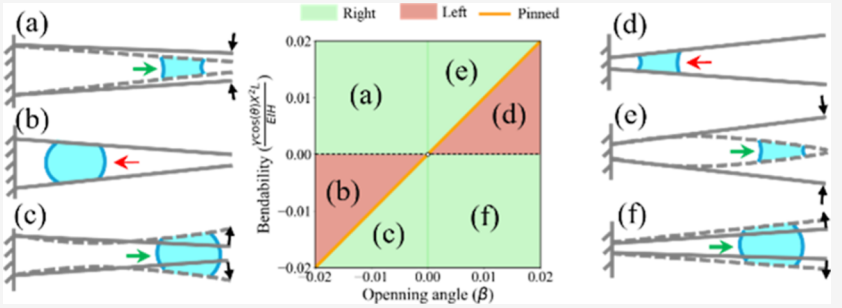

ABSTRACT: Spontaneous and directional droplet transport has attracted considerable attention for its potential applications such as self-cleaning surfaces and microfluidics. Previous studies on the droplet motion between rigid or parallel flexible channels established that the movement direction can be predetermined by the initial channel configuration and wettability. However, in this study, we experimentally show that the direction of droplet movement in nonparallel deformable channels can be carefully tuned, even under the same geometric and wetting conditions. This advanced feature arises from the interplay between initial system conditions and the subsequent solid−liquid interaction, depending on the initial channel configuration, channel flexibility, droplet conditions, wettability, and contact angle hysteresis. Combining the capillary pressure determined from the Young−Laplace equation with the structural deformation described by Euler−Bernoulli beam theory, we developed a general mathematical model capable of accurately predicting the droplet movement direction under a wide range of conditions. The model does not need any fitting parameters and is validated by our experiments. Additionally, our results lead to the identification of a phase diagram encompassing three distinct modes of droplet movement: toward the free end, toward the fixed end, and a stationary state. The proposed phase diagram serves as a predictive tool, offering new insights into controlling the direction of spontaneous droplet motion in flexible channels, with applications in the design and optimization of microfluidic devices.

1. INTRODUCTION

The controlled transport of droplets has gained considerable attention in recent decades due to its potential in advancing innovative technologies, including microfluidics,[1] self-cleaning surface,[2] antifogging,[3] hairy coating,[4] and medical diagnostics.[5] There is especially growing interest in spontaneous droplet transport mechanisms inspired by biology. For instance, insects like the water strider can self-remove water from their legs,[4] certain birds can hydrate by adjusting the beak opening angle,[6] some others are using the tongue structure to pick up a liquid,[7] and some plants can transport liquids through specialized surface structures on their leaves or shoots.[8,9] These spontaneous transport mechanisms rely solely on structural features rather than requiring additional external energy inputs such as surface charge.[10]

These mechanisms can be broadly categorized into two types. The first relies on rigid geometries, such as positioning droplets within wedges,[11] atop cones,[12] and converging capillary.[13] Relevant studies indicate that the droplet movement direction is strongly influenced by the interplay between the channel geometry and droplet wettability. For instance, hydrophilic droplets (*i.e.*, contact angle $\theta < 90°$) typically move toward narrower ends,[6] while hydrophobic (*i.e.*, $\theta > 90°$) droplets tend to migrate toward open ends.[11] This observation underscores the importance of investigating the coupled effects of the channel geometry and wettability on droplet transport. The second one involves inducing motion through the deformation of solid boundaries, exemplified by processes like *durotaxis*[14] and *tensotaxis*,[15] where gradients in substrate stiffness or stress drive droplet motion.

Received: November 15, 2024
Revised: March 3, 2025
Accepted: March 5, 2025
Published: March 14, 2025

Recently, a novel passive droplet transport mechanism known as *bendotaxis* has been explored for achieving wettability-independent spontaneous droplet transport. This mechanism involves sandwiching a droplet between two parallel flexible channels, with one end clamped and the other free.[16] A key feature of this mechanism is the coupling between the capillary-induced bending and droplet movement, which makes the transport direction independent of the wetting condition, *i.e.*, the droplet moves toward the free end regardless of wettability. Nevertheless, the coupled effects of the initial configuration and bendability of the channel can significantly influence droplet movement behavior and may even reverse its direction.[4,6,17] Prior studies of *bendotaxis* have primarily focused on parallel channel configurations, potentially overlooking a wider spectrum of droplet motion phenomena.

The aforementioned studies, as summarized in Table 1, have established that the droplet movement direction is determined once the solid system and wettability are chosen. However, in the present work, where deformable geometries are introduced, the movement direction can be opposite even with the same geometric configuration (*e.g.*, a positive opening angle) and wetting condition (*e.g.*, hydrophilic). This deviation highlights the complexity of droplet behaviour in flexible systems, where initial channel configuration, channel bendability, wettability, and contact angle hysteresis interact to influence movement. To address this, we first developed a mathematical model incorporating contact angle hysteresis to predict the direction of droplet motion. By analyzing the pressure gradient along the droplet, three distinct moving modes were identified: left (*i.e.*, move toward fix end), right (*i.e.*, move toward free end), and pinned (*i.e.*, stationary). Based on this, a phase diagram was proposed to predict droplet movement in nonparallel flexible channels. To validate the theoretical predictions, a custom-developed optical monitoring system was employed to conduct droplet-flexible channel experiments. The results showed a strong agreement with the proposed phase diagram. Our study extends the understanding of droplet transport in flexible channels by highlighting the significant roles of initial channel configuration, channel flexibility, droplet conditions, wettability, and contact angle hysteresis. These insights offer considerable potential for enabling tunable spontaneous droplet motion, with applications in the design and optimization of microfluidic devices.

Table 1. Summary of Mechanisms for Spontaneous Droplet Movement

mechanisms	solid deformability	movement direction when wettability changes[a]
wedge-shaped pattern[4]	×	opposite
roughness/wettability gradient[18,19]	×	opposite
conical structure[20]	×	same
durotaxis[14]	√	opposite
tensotaxis[15]	√	
bendotaxis[16]	√	same
current study	√	tunable

[a]Here "wettability changes" refers to a switch of wetting condition between hydrophilicity and hydrophobicity.

2. EXPERIMENTAL METHODS

A series of laboratory experiments were designed to understand the complexity of spontaneous droplet movement by considering the channel deformability (*i.e.*, coverslips with different Young's moduli), wettability (*i.e.*, contact angle), and channel configuration (*i.e.*, gap distance and opening angle).

2.1. Sample Preparation. Two types of glass coverslips were fabricated via laser cutting: (1) soda-lime glass (Young's modules $E = 7.5 \times 10^9$ Pa, thickness $b = 0.05$, 0.10, 0.15 mm) and (2) quartz glass (Young's modules $E = 7.5 \times 10^{11}$ Pa, thickness $b = 0.20$ mm). The channel length L_C and width w are 36 ± 0.1 mm and 5 ± 0.05 mm, respectively. Different surface treatments were applied to the substrates to control the surface wettability, as decribed below.

2.1.1. Hydrophilic Surface Treatment. To realize a consistent hydrophilic surface treatment, the ion-assisted plasma polymerization (IAPP) process was employed to induce the desired ranges of contact angle and reduce the contact angle hysteresis.[21]

First, the substrate underwent ultrasonic cleaning in acetone and subsequent cleaning in ethanol at 20 °C for 20 min each, followed by rinsing with Milli-Q water. The samples were then air-dried at room temperature for subsequent deposition of the ion-assisted plasma-polymerized film (IAPPF). A custom-built plasma polymerization apparatus was used. Comprehensive descriptions of the various components of this system are available in previous studies.[22,23]

Prior to the film deposition, a plasma argon (Ar) cleaning process was conducted under vacuum conditions with a base pressure of 5×10^{-5} Torr, a working pressure of 8×10^{-2} Torr, and a gas flow rate of 40 standard cubic centimeters per minute (sccm) of Ar. This cleaning step involved generating a radio frequency power of 50 W using an ENI radiofrequency power supply (13.56 MHz) to initiate plasma. Simultaneously, a negative bias voltage of 500 V was applied in a pulsed manner with a pulse width and frequency of 20 μs and 3 kHz, respectively, to the substrate holder via a RUP-6 pulse generator (GBS Elektronik GmbH) for 10 min. After the Ar cleaning, the chamber was pumped to approximately 5×10^{-5} Torr before introducing the gases for the film deposition. Subsequently, a mixture of acetylene (C_2H_2) in nitrogen (N_2) and Ar gases was injected into the system at constant flow rates of 5, 5, and 20 sccm, respectively. After the gases were introduced into the system, the working pressure was adjusted to 110 mTorr before applying an RF power of 50 W and a negative bias voltage of 500 V and the deposition lasted for 4 min.

2.1.2. Hydrophobic Surface Treatment. The hydrophobic treatment involved applying a commercial hydrophobic spray (Soft 99, Japan) to the coverslips in three successive layers. Each layer was dried under ambient conditions, with the first two drying for 30 minutes each and the final layer for 24 hours to ensure complete evaporation of isopropanol. This process produced a coating of hydrophobic nanoparticles on the surface, with a thickness negligible compared to that of the coverslip.[24]

2.2. Surface Wetting Behavior. The equilibrium contact angle θ_e of a 15 μL droplet on a horizontal coverslip was determined by analyzing microscopy images using the ImageJ contact angle plug-in.[25] Each measurement was repeated 10 times per sample to obtain an average value, ensuring that the standard deviation was below 5% to the desired contact angle. For the hydrophilic surface, following plasma treatment, it took approximately 7 days to reach the desired contact angle, after which it remained stable for 2−3 days. To monitor changes, the contact angle was measured twice a day after treatment. Once the desired contact angle was achieved, measurements were taken every 2 hours. Formal testing was initiated when the standard deviation in the contact angle across five consecutive measurements was less than 5%. The contact angles used in this study for hydrophilic surfaces were 39.73, 49.83, and 60.30°. For the hydrophobic surface, contact angle measurements were conducted after the treatment process, and two contact angles were employed: 106.11 and 121.03°. The detailed surface information is listed in Table 2.

2.3. Test Setup. In this study, a custom-developed optical monitoring system was employed to investigate the interaction between solid and liquid phases, as depicted in Figure 1a,b. The entire

https://doi.org/10.1021/acs.langmuir.4c04615
Langmuir 2025, 41, 7355−7363

Table 2. Summary of Surface Wettability Information

surface type number	wettability[a]	average contact angle (°)	standard deviation (°)
1	hydrophilic	39.73	0.976
2		49.83	1.234
3		60.30	1.092
4	hydrophobic	106.11	1.521
5		121.03	1.697

[a]Notes: Hydrophilic surface was treated by IAPPF and the hydrophobic surface was achieved by applying a commercial hydrophobic spray (Soft 99, Japan).

experimental setup was mounted on an optical platform (with a flatness of ±0.05 mm over 0.36 m^2) to ensure a uniform surface, with all components aligned at the same absolute height. The system comprises two key components: a geometry control system and a camera system. The geometry control system was designed to precisely position two glass plates at the specified location. It includes a motorized translation stage (Thorlabs, MTS50/M-Z8, with a home local accuracy of ±4 μm) for adjusting the gap distance between the coverslips, two goniometers (RUNJIA, GFG40-25X) calibrated by digital inclinometers (J.Y. Instruments, DXL360S) with an accuracy of 0.01° for fine-tuning the opening angle β, and two high-precision aluminum alloy supports (manufactured to International Tolerance grade IT6) to securely hold the coverslips in place. The camera system consists of a high-uniformity LED light source (JSIONX, JS-DBL105-105) aligned parallel to the coverslips and a digital microscope (HiROX, MXB-050Z) positioned on the opposite side. This configuration enables the capture of both the coverslip geometry and liquid motion at a rate of 30 frames per second.

2.4. Test Procedures. First, the flexible channels with the desired contact angle were secured to the high-precision supports and fixed to the goniometers. Second, both goniometers were calibrated to the target opening angle (β), defined as the angle between the upper coverslip and horizontal line, with positive values indicating an upward tilt. The opening angle for the bottom coverslip is reversed, as denoted in Figure 1c, and connected to the high-precision supports. Third, the translation stage was adjusted until either the fixed or free ends of the coverslips made contact, establishing the initial position. Fourth, the translation stage was raised to a specific height (*e.g.*, 8 mm) to provide sufficient space for a micropipette with a narrow syringe tip to inject a liquid droplet (*i.e.*, deionized water) of volume V attaching the bottom coverslip. Finally, the translation stage was motorized to move at a constant speed until the coverslips reached the desired gap distance, enabling the intended behaviors under testing conditions. Figure 1c,d shows the initial droplet condition just before movement begins. The top view of the droplet (Figure 1d) shows that the contour of the contact lines is not straight. However, while calculating the Gaussian curvature, the contribution of the out-of-plane component is two orders of magnitude larger than the in-plane curvature in this study, our 2D assumption still stands, and these curved contact lines can be ignored.

3. RESULTS AND DISCUSSION

3.1. Typical Modes of Droplet Motion. We first present three representative results of spontaneous droplet motion in diverging channels ($\beta > 0$) under different wettability conditions and initial droplet locations. In Case A (Figure 2a), the weakly hydrophilic droplet (surface 3, as shown in Table 2) location was positioned closer to the fixed end on a stiffer plate. As a result, the negative pressure within the droplet is insufficient to deform the solid, leaving the overall opening angle of the channels positive, which drives the droplet to move leftward. This outcome aligns with commonly observed phenomena in fixed structures.[6] In Case B (Figure 2b), when the surface becomes hydrophobic (Surface 4, as shown in Table 2), the pressure inside the droplet turns positive, causing the channels to deform outward. Simultaneously, the droplet moves spontaneously toward the wider region due to a net positive capillary force driving it to the right. Compared to Case A (Figure 2a), the movement direction reverses as the wettability changes, which matches expectations. However, when Case C is considered (Figure 2c), some discrepancies with previous studies become apparent. The strongly hydrophilic droplet (Surface 1, as shown in Table 2) creates negative pressure, pulling the channel walls toward the centerline. With the left end of the channel fixed, the resulting narrowing on the right further encourages the droplet to move rightward. Interestingly, despite reversed wettability compared to Case B (Figure 2b), the droplet moves in the same direction, contradicting the expectations of fixed geometry where movement would be reversed. These observations emphasize the significant influence of deformable structures on droplet motion. This behavior is somewhat reminiscent of *bendotaxis*, where both hydrophilic and hydrophobic droplets move toward the free end in deformable channels. However, comparing Case A (Figure 2a) with Case C (Figure 2c), despite both involving

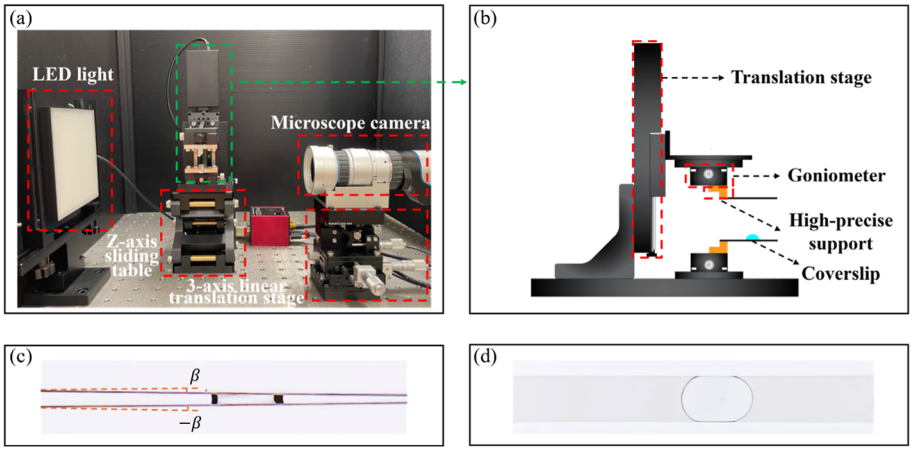

Figure 1. (a) Overview of the custom-developed optical monitoring system; (b) Schematic diagram of the droplet-flexible channel interaction platform; (c) Side view of a droplet spans the width of the channel; (d) Top view of a droplet between a flexible channel after deformation.

https://doi.org/10.1021/acs.langmuir.4c04615
Langmuir 2025, 41, 7355−7363

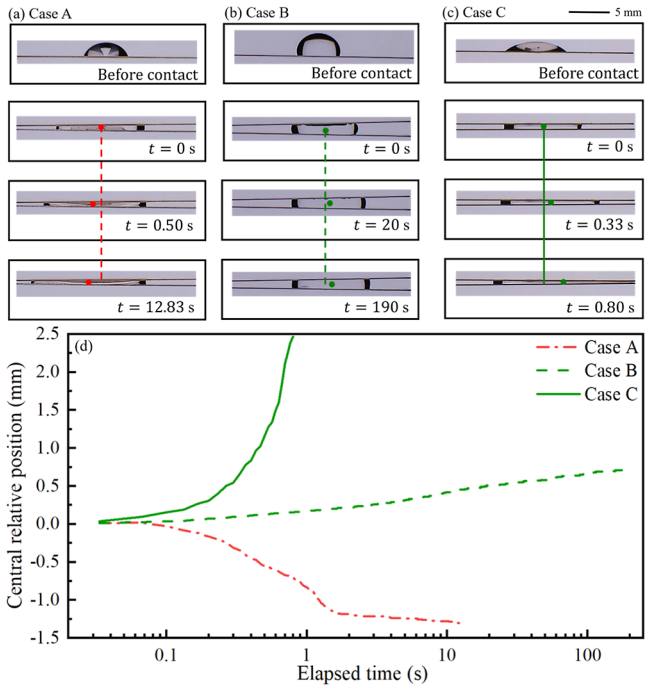

Figure 2. (a) Droplet motion process of Case A (L_C = 36 mm; w = 5 mm; b = 0.15 mm; β = 0.5°; X = 12 mm; V = 15 μL; H = 0.309 mm; θ = 60°); (b) Droplet motion process of Case B (L_C = 36 mm; w = 5 mm; b = 0.15 mm; β = 0.8°; X = 24 mm; V = 40 μL; H = 0.820 mm; θ = 105°); (c) Droplet motion process of Case C (L_C = 36 mm; w = 5 mm; b = 0.15 mm; β = 0.5°; X = 24 mm; V = 20 μL; H = 0.719 mm; θ = 40°); and (d) Droplet central position versus elapsed time. See Figure 3a for the system configuration and meaning of notations.

deformed structures, the droplets move in opposite directions, which does not align with the previous findings. This suggests a broader range of droplet motion phenomena in flexible channels with varying opening angles that remains underexplored. The rich dynamics discussed above highlight the complex coupling between the liquid motion and solid deformation. In the next section, we develop a theoretical model based on the competition between the opening angle and solid bendability to determine the liquid movement behavior.

3.2. Mathematical Model. The schematic of the system considered in the mathematical model is illustrated in Figure 3a. Two flexible coverslips with Young's modules E, width w, thickness b, and length L_s are fixed at the left end forming an opening angle β. The fixed end is defined as the y-axis and the center line of the channel defines as the x-axis, with the origin (x,y) = (0,0) being located at the center of the fixed end. Accordingly, the flexible boundaries are described by the equation $y = \pm h(x)$. A droplet with volume V, surface tension γ, and contact angle θ is initially placed at location $(X\cdot\cos\beta, 0)$ that forms a liquid bridge between the flexible boundaries extending from x^- to x^+. The distance between the two coverslips at the midpoint between x^- and x^+ is denoted as H. To simplify the system, this model is based on the following main assumptions:

(1) Because $w/L \ll 1$, a 2D model is considered and the analysis is conducted in the (x,y)-plane.
(2) The effect of gravity is neglected. Given that the bond number $\rho g H_0^2/\gamma = 5.38\cdot10^{-9} \sim 1.09\cdot10^{-7} \ll 1$, the surface tension dominates the droplet motion.[26]
(3) Evaporation is not considered. As the time scale of evaporation (~hours) is much longer than the capillary time scale (~seconds), especially for a confined droplet, the evaporation can be neglected.[6,27]
(4) The droplet length is much smaller than the coverslip length $L/L_s \ll 1$, the force applied from the droplet on the flexible walls is simplified as an effective point force at the center of the liquid−solid contact line.

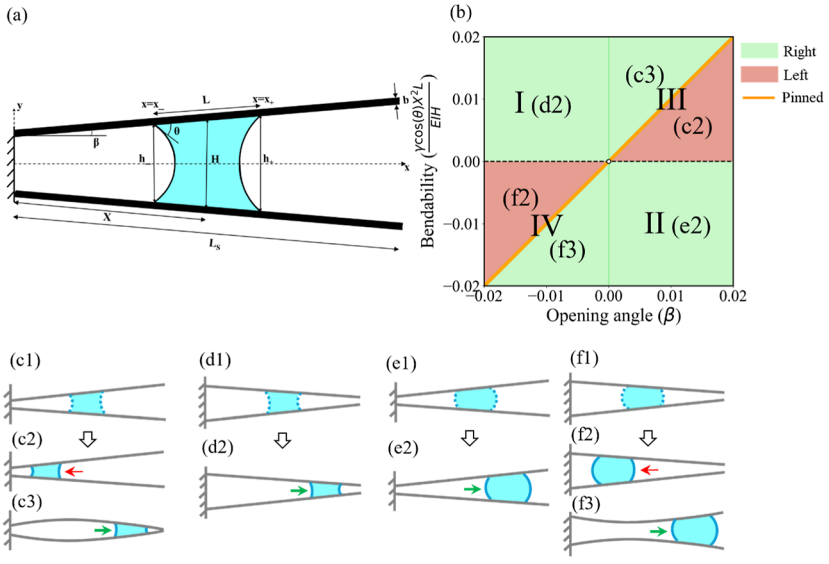

Figure 3. (a) Schematic of a droplet in a flexible channel. The fixed boundary is located at x = 0. Two deformable walls of length L_s open at an angle β, with thickness b and separation H at $x = X\cdot\cos\beta$. The droplet is initially located at X, making contact with the walls at perpendicular distances $x = x^-$ and $x = x^+$, forming a contact angle θ; (b) Theoretical phase diagram for droplet motion with no contact angle hysteresis; (c1−c3) Initial configuration where $\beta > 0$ and possible motions of a hydrophilic droplet ($0 < \theta < 90°$) in this configuration; (d1,d2) Initial configuration where $\beta < 0$ and possible motion of a hydrophilic droplet ($0 < \theta < 90°$) in this configuration; (e1,e2) Initial configuration where $\beta > 0$ and possible motion of a hydrophobic droplet ($90 < \theta < 180°$) in this configuration; and (f1−f3) Initial configuration where $\beta < 0$ and possible motions of a hydrophobic droplet ($90 < \theta < 180°$) in this configuration.

https://doi.org/10.1021/acs.langmuir.4c04615
Langmuir 2025, 41, 7355−7363

(5) At the instance of droplet formation after the linear stage reaches the targeted range, we assume that the solid channel deforms much faster than the subsequent droplet motion.

3.2.1. Capillary Force. In this model, the flexible boundaries are assumed to be initially undeformed. The length of the droplet (which also corresponds to the length of liquid−solid contact lines) satisfies:

$$L = \frac{V}{w \cdot H} \tag{1}$$

This leads to the local channel spacing at the left and right sides of the droplet (denoted by subscripts "−" and "+", respectively) being:

$$h_{-} = H - L \cdot \tan \beta \tag{2a}$$

$$h_{+} = H + L \cdot \tan \beta \tag{2b}$$

With a given equilibrium contact angle θ_e, the curvatures of the menisci geometrically satisfy $\kappa_{\pm} = 2 \cos \theta_e / h_{\pm}$ with the mean curvature $\kappa = 2 \cos \theta_e / H$. Consequently, the effective point force on the coverslips at the initial stage is calculated as:

$$F = \gamma \kappa L = -\frac{2\gamma L \cos \theta_e}{H} \tag{3}$$

and its position is at X initially.

3.2.2. Beam Deflection Model. Considering the coverslips are thin, *i.e.*, $w \ll L$ and its deflection is small, *i.e.*, $\Delta H \ll L$, the shear deformation and rotational inertial can be ignored and thus the Euler−Bernoulli beam theory is adopted to describe the mechanics of coverslips. The displacement u can be solved from the following governing equation:

$$\frac{d^2 u}{dx^2} = \frac{M(x)}{B} \tag{4}$$

where $M(x) = F(x - X)$ is the moment at x, $B = \frac{Eb^3}{12}$ represents the bending stiffness. As the flexible channels are fixed at $x = 0$, hence, the boundary conditions are $\frac{du}{dx}|_{x=0} = \beta$ and $u|_{x=0} = 0$. The deflection (ΔH) and the variations in the opening angle $(\Delta \beta)$ at specific location X are therefore:

$$\Delta H = \frac{FX^3}{3B} \tag{5}$$

$$\Delta \beta = \frac{FX^2}{2B} \tag{6}$$

The opening angle and gap distance after deformation are then updated:

$$\beta' = \beta + \Delta \beta \tag{7}$$

$$H' = H + \Delta H \tag{8}$$

The droplet length and local channel spacing at the left and right sides of the droplet can be updated accordingly via eqs 1 ,2a and 2b:

$$L' = V/(w \cdot H') \tag{9}$$

$$h'_{-} = H' - L' \cdot \tan \beta' \tag{10a}$$

$$h'_{+} = H' + L' \cdot \tan \beta' \tag{10b}$$

3.2.3. Contact Angle Hysteresis. Special attention is required for the variation in contact angles during the droplet movement, where the effective contact angles at the advancing (θ_a) and receding (θ_r) sides can be different due to the contact angle hysteresis.[26] In practical applications such as manufacture of self-cleaning surfaces, considerable efforts are made to reduce contact angle hysteresis.[12] Theoretically, the contact angle hysteresis is often neglected entirely.[16] However, achieving ideal surface conditions in practice is challenging, and some degree of hysteresis is inevitable. In scenarios involving passive droplet motion, because the driving force (capillary force) is highly sensitive to the wetting condition, the existence of contact angle hysteresis may contribute to significant resistance to fluid motion, potentially preventing the movement process.[6] Here, we adopt a simple model that allows for different advancing and receding angles.[28] It should be noted that the contact angles often exhibit a dynamic response with respect to the capillary number.[29,30] In this study, the capillary number is less than 7×10^{-5}, allowing us to ignore the additional effects from a dynamic contact angle hysteresis.

Thus, we further assume that (1) the droplet-channel system has intrinsic stationary advancing and receding contact angles; (2) a dynamic meniscus has a constant contact angle equal to θ_a, if the meniscus is advancing (liquid-invading-vapor) or θ_r if the meniscus is receding (vapor−invading−liquid). For notational convenience, a dimensionless parameter λ is introduced to quantify the contact angle hysteresis:

$$\lambda = \frac{\cos \theta_r}{\cos \theta_a} - 1 \tag{11}$$

where $\cos \theta_r$ and $\cos \theta_a$ are the contact angles at the receding and advancing fronts, respectively. It should be noted that both θ_r and θ_a should lie within either range $[0, 90°)$ or $(90, 180°]$, depending on the specific conditions. A value of $\lambda = 0$ represents equal contact angles at both menisci, corresponding to the case with no contact angle hysteresis.

3.2.4. Determining Droplet Movement Direction. The movement direction is defined by the variation in the central position: $0.5 \cdot (x^+ + x^-)$.

After deformation, the corresponding pressures at the left and right menisci are given by:

$$p_{\pm} = \frac{-\gamma \cos \theta}{h'_{\pm}} \tag{12}$$

Here, $\theta = \theta_r$, if the meniscus is receding; $\theta = \theta_a$, if the meniscus is advancing; and $\theta = \theta_e$, if the contact angle hysteresis is not considered.

When neglecting the effects of contact angle hysteresis (*i.e.*, $\lambda = 0$), the pressure difference across the droplet will drive it in the direction of the pressure gradient, which can be expressed as:

$$\Delta p = \frac{-\gamma \cos \theta_e}{0.5 \cdot h'_{+}} - \frac{-\gamma \cos \theta_e}{0.5 \cdot h'_{-}} \tag{13}$$

Based on this equation, it can determine the direction of droplet movement: (1) if $\Delta p < 0$, the droplet moves toward the positive x-direction (free end on the right side); (2) if $\Delta p > 0$, the droplet moves toward the negative x-direction (fixed end on the left side); and (3) if $\Delta p = 0$, the droplet is pinned and stays stationary, and the pinned boundary can be written as:

https://doi.org/10.1021/acs.langmuir.4c04615
Langmuir 2025, 41, 7355−7363

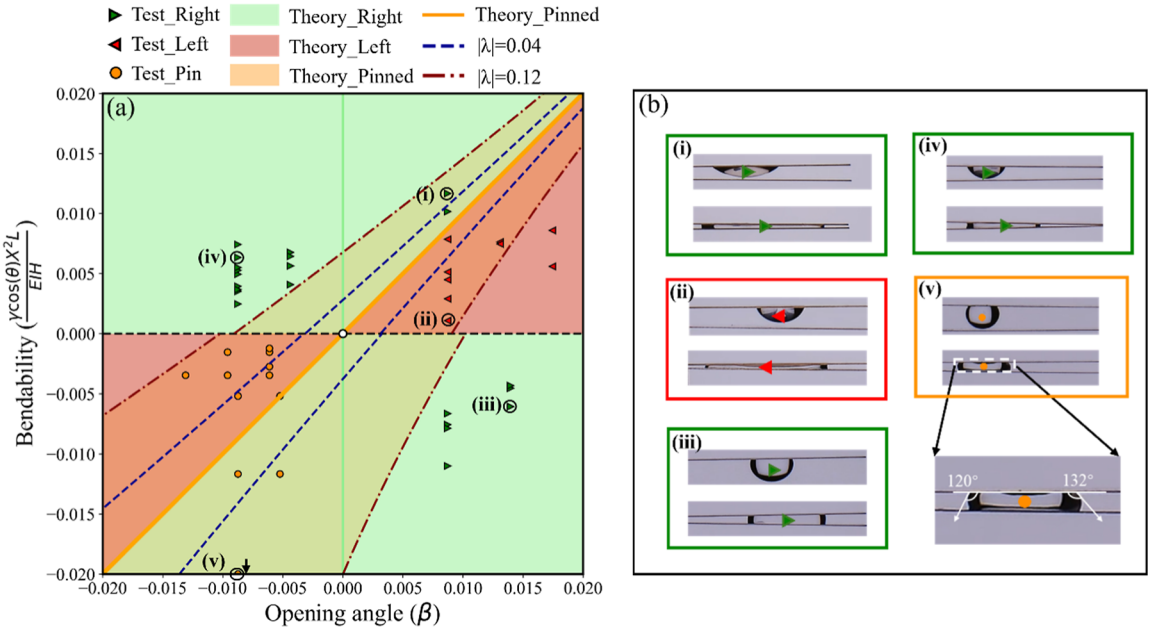

Figure 4. (a) Phase diagram for droplet motion in flexible channels (the background and lines represent theoretical predictions, and the points indicate experimental results). (b) Representative test results across different combinations of wettability and initial configurations.

$$\beta = -\Delta\beta \tag{14}$$

When incorporating the effects of contact angle hysteresis (*i.e.*, $\lambda \neq 0$), we introduce the aforementioned dimensionless parameter λ (as shown in eq 11). Using the "left" motion as a demonstration, the contact angle at the right meniscus θ_+ should correspond to the receding angle θ_r:

$$\cos\theta_+ = \cos\theta_r = (\lambda + 1)\cos\theta_a \tag{15}$$

Hence, the pressure difference can be written as:

$$\Delta p = \frac{-\gamma(\lambda + 1)\cos\theta_a}{0.5\cdot h'_+} - \frac{-\gamma\cos\theta_a}{0.5\cdot h'_-} \tag{16}$$

If the droplet moves toward the fixed end on the left side without accounting for the contact angle hysteresis, it should initially satisfy the condition: $p_- < p_+$. After the contact angle hysteresis is incorporated, if Δp remains positive, the droplet continues to move toward the left. However, if $\Delta p \leq 0$, the driving force is smaller than the adhesive force, resulting in the droplet being pinned and unable to move.[31] If Δp shifts to a nonpositive value, the geometry of flexible channels derived from eq 16 should, therefore, satisfy the following conditions:

$$(\lambda + 1)h'_- \geq h'_+, \qquad \theta \in [0^\circ, 90^\circ) \tag{17a}$$

$$(\lambda + 1)h'_- \leq h'_+, \qquad \theta \in (90^\circ, 180^\circ] \tag{17b}$$

Combining eqs 17a and 17b with eqs 10a and 10b, the boundaries for pinned cases should yield:

$$\beta \leq -\Delta\beta + \frac{\lambda\cdot\omega}{(\lambda + 2)V}\left(H^2 + \frac{8}{3}\cdot X\cdot H\cdot\Delta\beta + \frac{16}{9}\cdot X^2\cdot\Delta\beta^2\right), \qquad \theta \in [0^\circ, 90^\circ) \tag{18a}$$

$$\beta \geq -\Delta\beta - \frac{\lambda\cdot\omega}{(\lambda + 2)V}\left(H^2 + \frac{8}{3}\cdot X\cdot H\cdot\Delta\beta + \frac{16}{9}\cdot X^2\cdot\Delta\beta^2\right), \qquad \theta \in (90^\circ, 180^\circ] \tag{18b}$$

The derivations for right-moving cases follow a similar process. For the sake of brevity, the pinned range is provided directly here:

$$\beta \geq -\Delta\beta - \frac{\lambda\cdot\omega}{(\lambda + 2)V}\left(H^2 + \frac{8}{3}\cdot X\cdot H\cdot\Delta\beta + \frac{16}{9}\cdot X^2\cdot\Delta\beta^2\right), \qquad \theta \in [0^\circ, 90^\circ) \tag{19a}$$

$$\beta \leq -\Delta\beta + \frac{\lambda\cdot\omega}{(\lambda + 2)V}\left(H^2 + \frac{8}{3}\cdot X\cdot H\cdot\Delta\beta + \frac{16}{9}\cdot X^2\cdot\Delta\beta^2\right), \qquad \theta \in (90^\circ, 180^\circ] \tag{19b}$$

Note that the boundaries describing the pinned regimes will depend on the specific conditions of the droplet position and the corresponding positions of the menisci within a given system.

3.2.5. Predicting Droplet Moving Modes. Based on the mathematical model, with the input parameters including contact angle, surface tension, contact angle hysteresis, initial droplet location, droplet volume, channel elastic modules, channel thickness, gap distance, and opening angle, the droplet movement direction can be determined. By examining the proposed model, it is found that the direction of droplet motion ultimately depends on two key parameters (1) the initial opening angle β at the fixed end and (2) $\Delta\beta$, referred to as bendability, which quantifies the extent of channel deflection under given conditions. The theoretical droplet moving modes are denoted in Figure 3b. The background colors, red and green represents the predicted droplet movements to the left and right, respectively, as derived from the model. When $\Delta\beta = 0$ (*i.e.*, $y = 0$), which corresponds to conditions where the channel stiffness approaches infinite or zero surface tension, this scenario is the extreme case for the discussion below. Within this framework, the droplet motion can be discussed in detail across the following scenarios.

3.2.5.1. Without Contact Angle Hysteresis $\lambda = 0$. $\beta < 0$, $0^\circ < \theta < 90^\circ$ (I) in Figure 3d1,d2 and $\beta > 0$, $90^\circ < \theta < 180^\circ$ (II) in

https://doi.org/10.1021/acs.langmuir.4c04615
Langmuir 2025, 41, 7355−7363

Figure 3e1,e2: as these two cases induce pressure gradients toward the free end after the liquid−solid contact, the droplet will undoubtedly move in that direction.

$\beta > 0$, $0° < \theta < 90°$ (III) in Figure 3c1−c3 and $\beta < 0$, $90° < \theta < 180°$ (IV) in Figure 3f1−f3: the droplet moving direction depends on the relation between channel bendability and opening angle. For scenario (III), if $\beta > \Delta\beta$, it generates pressure gradients toward the fixed end, causing the droplet to move left (Figure 3c2). Once the condition shifts to $\beta < \Delta\beta$, the direction of pressure gradient will reverse, leading the droplet to move right (Figure 3c3). In scenario (IV), due to the reversed Laplace pressure induced by wettability, the movement direction determination is also reversed: if $\beta < \Delta\beta$, droplet will move left (Figure 3f2) and when the $\beta > \Delta\beta$ droplet will move right (Figure 3f3).

$\beta = -\Delta\beta$ (V): droplet meets the pinned condition, presented as the yellow solid line. After the deformation caused by the solid−liquid contact, the droplet remains stationary.

$\beta = 0$ (VI) (*i.e.*, *y* axis): if a wetting (or nonwetting) droplet is injected between the parallel flexible channels, the negative (or positive) Laplace pressure deforms the channels inward (or outward). The deformation is larger at the meniscus near the free end than at the fixed end, creating a pressure gradient toward the free end that drives the droplet along the same direction (*i.e.*, right movement in this work). This type of wettability-independent spontaneous droplet motion in parallel flexible channels is known as *bendotaxis*, which has been both experimentally and theoretically validated.[16]

3.2.5.2. With Contact Angle Hysteresis $\lambda \neq 0$. **Contact angle hysteresis-induced pinned regime (VII)**: If the contact angle hysteresis-induced adhesive force exceeds the driving force, the droplet becomes pinned between the flexible channels. As the boundaries indicated by eqs 18a, 18b, 19a, and 19b, there will exist a pinned area, which is discussed in detail in the following section.

3.3. Comparisons with Experimental Results. To thoroughly examine the validity of the proposed model, a series of detailed experiments were conducted, covering parameters including Young's modules, E, gap distance, H, droplet volume, V, contact angle, θ, and inject location, X (*i.e.*, inject distance from fixed ends). The experimental results are summarized in Figure 4. Based on eqs 18a, 18b, 19a, and 19b, and considering fixed values for V, X and H, the pinned area can be identified. Here, using $V = 20\ \mu$L, $X = 12$ mm, and $H = 0.8$ mm, two λ values (*i.e.*, 0.04 and 0.12) are incorporated to account for varying degrees of contact angle hysteresis. The pinned areas are superimposed in yellow on the phase diagram, with the boundaries represented by blue dot lines ($\lambda = 0.04$) and red dot lines ($\lambda = 0.12$). As the λ increase, the pinned area also expands, which is in line with previous studies.[28] It should be noted that the contact angle hysteresis has the greatest impact on droplet pinning in scenario (IV), suggesting a high likelihood that most cases within this region will result in the droplet being pinned.

All test results are superimposed on the phase diagram, where red, green, and yellow dots denote leftward, rightward, and pinned droplet movements. For a better illustration, several representative examples are provided to show the initial conditions and movement directions: (1) the channel geometry and droplet central location before contact and (2) the droplet central location after contact, either after it has moved 10% of the total length or after 3 minutes. It is obvious that most experimental results align with theoretical predictions. The focus here will be on cases with $\beta < 0$ and $90° < \theta < 180°$. In these cases, all droplets are pinned, consistent with the theoretical predictions when the contact angle hysteresis is considered. As the example *v* shown in Figure 4b, even though the droplet is capable of deforming the flexible channel from negative β to positive β, the larger contact angle hysteresis (*i.e.*, $\lambda = 0.34$) causes the droplet to remain pinned after deformation. This large contact angle hysteresis is primarily due to surface treatment. Although a 3-step spray process is employed to minimize the hysteresis to the greatest extent, unlike IAPP, it is challenging to achieve a hysteresis-free or low-hysteresis hydrophobic surface in our experiments.

3.4. Discussion. Some comments can be made about the droplet motion analysis. In addition to the initial movement direction, the droplet moving speed is another important factor determining transport efficiency. In principle, by adding the additional dissipation terms, such as viscous effects during the transport,[16] the mathematical framework presented in this work should be capable of describing the temporal changes of position and velocity. However, this study does not provide further analysis regarding the moving velocity due to two primary limitations. First, the limited image resolution introduced fluctuations in the detected liquid boundary during image analysis processes, which significantly impacts the accuracy of velocity analysis and make it difficult to obtain reliable motion data. More importantly, surface heterogeneity cannot be completely removed. As the capillary-driven droplet motion is very sensitive to the effective contact angle, local variations in advancing/receding contact angles may lead to nonuniform movement, making cross-experimental comparisons unreliable. For example, as shown in Figure 2b, although the hydrophobic droplet is expected to stop until it reaches the free end, its motion terminates in the middle of the channel due to the obvious hysteresis effects. However, it is worth noting that motion shifts (*i.e.*, from moving left or right to pinning) caused by the contact angle hysteresis could offer new opportunities for passive droplet control, such as fine-tuning the stopping point by manipulating contact angle hysteresis and wettability gradients. Further research should focus on exploring the entire motion process using numerical simulations that account for varying degrees of contact angle hysteresis. These simulations would allow for more precise control through adjusting hysteresis, yielding valuable insights into its effect on droplet motion. Additionally, the mathematical model could be extended from an energy-based perspective to include factors, such as viscous dissipation, providing a more comprehensive understanding of the complexity interplays.

4. CONCLUSIONS

This study investigated the spontaneous droplet motion induced by solid−liquid interface interactions in flexible channels by accounting for the initial channel configuration, channel flexibility, droplet conditions, wettability, and contact angle hysteresis. Several key findings are listed below:

1. Unlike in rigid or parallel deformable systems where the droplet movement direction is predetermined by initial channel configuration and wettability, introducing flexible geometries can lead to opposite movement even under the same geometric and wetting conditions.

https://doi.org/10.1021/acs.langmuir.4c04615
Langmuir 2025, 41, 7355−7363

This complexity arises from the interplay of the system initial conditions and the subsequent solid−liquid interface interactions, depending on the initial channel configuration (*i.e.*, opening angle and gap distance), channel flexibility, droplet conditions (*i.e.*, volume and injection position), wettability, and contact angle hysteresis (described by λ). These tunable droplet motion behaviours have been validated through experiments conducted using a custom-developed optical monitoring system in this study.

2. This study proposes a mathematical model incorporating contact angle hysteresis to predict the initial droplet motion direction. The model does not require any fitting parameter and identifies three distinct modes of movement: toward the free end, toward the fixed end, and a stationary state. These predictive results have been successfully validated through experiments and synthesized into a phase diagram highlighting the modes and their corresponding conditions, thereby enhancing our understanding of the complex factors governing droplet transport in flexible channels.
3. Contact angle hysteresis has emerged as a critical factor in droplet dynamics, particularly in its ability to shift a moving droplet into a pinned state. The study reveals that the stationary region expands as the hysteresis parameter λ increases, with the most pronounced impact observed when $\beta < 0$ and the contact angle θ lies between 90 and 180°. In this range, droplets are more likely to become pinned, highlighting the importance of considering contact angle hysteresis in designing and optimizing droplet transport systems.

These findings provide deeper insight into the complex interplay among structural flexibility, surface wettability, and contact angle hysteresis in governing droplet transport. This enhanced understanding of solid−liquid interface interactions offers potential for controlling spontaneous droplet motion, with applications in the design and optimization of microfluidic devices.

AUTHOR INFORMATION

Corresponding Authors

Zhongzheng Wang − *School of Mechanical, Medical and Process Engineering, Faculty of Engineering, Queensland University of Technology, Brisbane, Queensland 4001, Australia*; Email: zhongzheng.wang@qut.edu.au

Yixiang Gan − *School of Civil Engineering, The University of Sydney, Sydney, New South Wales 2006, Australia*; orcid.org/0000-0002-9621-0277; Email: yixiang.gan@sydney.edu.au

Authors

Haiyi Zhong − *School of Civil Engineering, The University of Sydney, Sydney, New South Wales 2006, Australia*

Si Suo − *Department of Civil and Environmental Engineering, Imperial College London, London SW7 2AZ, U.K.*

Leila Mamizadeh Janghour − *School of Biomedical Engineering, Faculty of Engineering, The University of Sydney, Sydney, New South Wales 2006, Australia*

Behnam Akhavan − *School of Biomedical Engineering, Faculty of Engineering, The University of Sydney, Sydney, New South Wales 2006, Australia; School of Engineering, University of Newcastle, Callaghan, New South Wales 2308, Australia*; orcid.org/0000-0002-1599-658X

Complete contact information is available at: https://pubs.acs.org/10.1021/acs.langmuir.4c04615

Notes

The authors declare no competing financial interest.

REFERENCES

(1) Squires, T. M.; Quake, S. R. Microfluidics: Fluid physics at the nanoliter scale. *Rev. Mod. Phys.* **2005**, *77*, 977−1026.

(2) Neinhuis, C.; Barthlott, W. Characterization and distribution of water-repellent, self-cleaning plant surfaces. *Ann. Bot.* **1997**, *79*, 667−677.

(3) Mouterde, T.; Lehoucq, G.; Xavier, S.; Checco, A.; Black, C. T.; Rahman, A.; Midavaine, T.; Clanet, C.; Quéré, D. Antifogging abilities of model nanotextures. *Nat. Mater.* **2017**, *16*, 658−663.

(4) Wang, Q.; Yao, X.; Liu, H.; Quéré, D.; Jiang, L. Self-removal of condensed water on the legs of water striders. *Proc. Natl. Acad. Sci. U. S. A.* **2015**, *112*, 9247−9252.

(5) Yager, P.; Edwards, T.; Fu, E.; Helton, K.; Nelson, K.; Tam, M. R.; Weigl, B. H. Microfluidic diagnostic technologies for global public health. *Nature* **2006**, *442*, 412−418.

(6) Prakash, M.; Quéré, D.; Bush, J. W. Surface tension transport of prey by feeding shorebirds: the capillary ratchet. *Science* **2008**, *320*, 931−934.

(7) Rico-Guevara, A.; Rubega, M. A. The hummingbird tongue is a fluid trap, not a capillary tube. *Proc. Natl. Acad. Sci. U. S. A.* **2011**, *108*, 9356−9360.

(8) Feng, S.; Zhu, P.; Zheng, H.; Zhan, H.; Chen, C.; Li, J.; Wang, L.; Yao, X.; Liu, Y.; Wang, Z. Three-dimensional capillary ratchet-induced liquid directional steering. *Science* **2021**, *373*, 1344−1348.

(9) Yang, L.; Li, W.; Lian, J.; Zhu, H.; Deng, Q.; Zhang, Y.; Li, J.; Yin, X.; Wang, L. Selective directional liquid transport on shoot surfaces of Crassula muscosa. *Science* **2024**, *384*, 1344−1349.

(10) Fang, D.; Zhou, W.; Jin, Y.; Liu, X.; Zeng, Y.; Wang, Z.; Zheng, H. Programmable droplet manipulation enabled by charged-surface pattern reconfiguration. *Droplet* **2023**, *2*, No. e74.

(11) Wang, Z.; Owais, A.; Neto, C.; Pereira, J. M.; Gan, Y. Enhancing spontaneous droplet motion on structured surfaces with tailored wedge design. *Adv. Mater. Interfaces* **2021**, *8*, 2000520.

(12) McCarthy, J.; Vella, D.; Castrejón-Pita, A. A. Dynamics of droplets on cones: self-propulsion due to curvature gradients. *Soft Matter* **2019**, *15*, 9997−10004.

(13) Singh, M.; Kumar, A.; Khan, A. R. Capillary as a liquid diode. *Phys. Rev. Fluids* **2020**, *5*, 102101.

(14) Bueno, J.; Bazilevs, Y.; Juanes, R.; Gomez, H. Wettability control of droplet durotaxis. *Soft Matter* **2018**, *14*, 1417−1426.

(15) Bueno, J.; Bazilevs, Y.; Juanes, R.; Gomez, H. Droplet motion driven by tensotaxis. *Extreme Mech. Lett.* **2017**, *13*, 10−16.

(16) Bradley, A. T.; Box, F.; Hewitt, I. J.; Vella, D. Wettability-independent droplet transport by Bendotaxis. *Phys. Rev. Lett.* **2019**, *122*, 074503.

(17) Kim, H. Y.; Mahadevan, L. Capillary rise between elastic sheets. *J. Fluid Mech.* **2006**, *548*, 141−150.

(18) Sun, C.; Zhao, X. W.; Han, Y. H.; Gu, Z. Z. Control of water droplet motion by alteration of roughness gradient on silicon wafer by laser surface treatment. *Thin Solid Films* **2008**, *516*, 4059−4063.

(19) Liu, C.; Sun, J.; Li, J.; Xiang, C.; Che, L.; Wang, Z.; Zhou, X. Long-range spontaneous droplet self-propulsion on wettability gradient surfaces. *Sci. Rep.* **2017**, *7*, 77552.

(20) Chen, C.; Liu, J.; Liu, Y.; Peng, X. Simulation investigation of the spontaneous motion behaviors of underwater oil droplets on a conical surface. *Soft Matter* **2022**, *18*, 9172−9180.

(21) Santos, M.; Filipe, E. C.; Michael, P. L.; Hung, J.; Wise, S. G.; Bilek, M. M. Mechanically robust plasma-activated interfaces optimized for vascular stent applications. *ACS Appl. Mater. Interfaces* **2016**, *8*, 9635−9650.

(22) Akhavan, B.; Croes, M.; Wise, S. G.; Zhai, C.; Hung, J.; Stewart, C.; Ionescu, M.; Weinans, H.; Gan, Y.; Amin Yavari, S.; Bilek, M. M.

Radical-functionalized plasma polymers: Stable biomimetic interfaces for bone implant applications. *Appl. Mater. Today* **2019**, *16*, 456−473.
(23) Sharifahmadian, O.; Zhai, C.; Hung, J.; Shineh, G.; Stewart, C. A.; Fadzil, A. A.; Ionescu, M.; Gan, Y.; Wise, S. G.; Akhavan, B. Mechanically robust nitrogen-rich plasma polymers: Biofunctional interfaces for surface engineering of biomedical implants. *Mater. Today Adv.* **2021**, *12*, 100188.
(24) Bradley, A. Droplet Transport by Bendotaxis. Doctoral Dissertation, University of Oxford, 2020.
(25) Schneider, C. A.; Rasband, W. S.; Eliceiri, K. W. NIH Image to ImageJ: 25 years of image analysis. *Nat. Methods* **2012**, *9*, 671−675.
(26) Gennes, P. G.; Brochard-Wyart, F.; Quéré, D. *Capillarity and Wetting Phenomena: Drops, Bubbles, Pearls, Waves*; Springer: New York, 2004.
(27) Hu, H.; Larson, R. G. Evaporation of a sessile droplet on a substrate. *J. Phys. Chem. B* **2002**, *106*, 1334−1344.
(28) Bradley, A. T.; Hewitt, I. J.; Vella, D. Droplet trapping in bendotaxis caused by contact angle hysteresis. *Phys. Rev. Fluids* **2021**, *6*, 114003.
(29) Blake, T. D.; Haynes, J. M. Contact-angle hysteresis. *Prog. Surf. Membr. Sci.* **1973**, *6*, 125−138.
(30) Shi, Z.; Zhang, Y.; Liu, M.; Hanaor, D. A.; Gan, Y. Dynamic contact angle hysteresis in liquid bridges. *Colloids Surf., A* **2018**, *555*, 365−371.
(31) Huang, X.; Li, Y.; Fan, J.; Wu, H.; Wang, F. Impeding effect on droplet spreading by a groove on the substrate. *Capillarity* **2024**, *13*, 1−9.

https://doi.org/10.1021/acs.langmuir.4c04615
Langmuir 2025, 41, 7355−7363